Journal of Alloys and Compounds 952 (2023) 170024

Contents lists available at ScienceDirect

Journal of Alloys and Compounds

journal homepage: www.elsevier.com/locate/jalcom

A strategy to regulate the yield ratio of a metastable high Zr-containing β titanium alloy: Synergistic effects of the β domain, β stability and β/α interfaces by varying the α phase content

Xiaoli Zhao [a,b,c,*], Rongxin Zhu [a], Wenke Song [a], Lei Meng [b], Mitsuo Niinomi [d,e,f,g], Takayoshi Nakano [e], Nan Jia [a], Deliang Zhang [a]

[a] School of Materials Science and Engineering, Northeastern University, Shenyang 110819, PR China
[b] National Frontiers Science Center for Industrial Intelligence and Systems Optimization, Northeastern University, Shenyang 110819, PR China
[c] Key Laboratory of Data Analytics and Optimization for Smart Industry (Ministry of Education), Northeastern University, Shenyang 110819, PR China
[d] Institute for Materials Research, Tohoku University, Sendai, Miyagi 980-8577, Japan
[e] Department of Materials and Manufacturing Science, Graduate School of Engineering, Osaka University, Suita 565-0871, Japan
[f] Department of Materials Science and Engineering, Faculty of Science and Technology, Meijo University, Nagoya 468-8502, Japan
[g] Department of Chemistry and Materials Engineering, Faculty of Chemistry, Materials and Bioengineering, Kansai University, Suita 564-8680, Japan

ARTICLE INFO

Article history:
Received 16 January 2023
Received in revised form 27 March 2023
Accepted 6 April 2023
Available online 7 April 2023

Keywords:
Metastable titanium alloy
Yield ratio
Deformation-induced phase transformation
α′ phase
Mechanical properties

ABSTRACT

To meet the demands of both processing and serving, to the best of our knowledge, this is the first report exhibiting large range control of the yield ratio from 0.31 to 0.96 with decent elongations over 10% in the same alloy with low-cost thermal treatments. The yield ratio of the metastable Ti-30Zr-5Mo alloy was regulated via adjusting trigger stress of the stress-induced phase transformation and work-hardening ability through changing the α phase content. Materials with acicular α phase of different contents were successfully prepared via low-cost thermal treatment. The effects of the α phase content on the stress-induced α′ martensite phase transformation and work hardening behavior were then investigated. In the Ti-30Zr-5Mo alloy with dual phases, due to the crystal difference and element partitioning, the hardness of the α phase is higher than that of the β matrix, and the hardness difference between the phases increases with increasing α phase. In addition to Mo, Zr plays an important role in stabilizing the β phase in high-Zr-containing alloys. Deformation initiates in the β phase of both single-phase and duplex-phase alloys. The deformation mechanism of the β phase is dependent on both the β domain and β stability. Due to the low trigger stress and excellent work hardening ability, stress-induced α′ martensite phase transformation is helpful to lower the yield ratio. As the α phase content increases, the trigger stress increases, and when the α phase content increases to 40%, dislocation slip dominates rather than stress-induced α′ martensite phase transformation, and a high yield strength of 944 MPa is obtained. The α/β phase interfaces act as effective obstacles to hinder dislocation movement and provide working hardening, and the obstruction effect is more significant with an increase in the hardness difference between the α and β phases. The stress-induced α′ phase transformation and/or the deformation coordination between the α and β phases guarantee decent elongations of no less than 10% in the large control of the yield ratio from 0.31 to 0.96 with a yield strength from 254 to 1013 MPa. It paves the way to develop “Unititaniam” alloys for wide possible applications.

1. Introduction

The yield ratio, which is the ratio of the yield strength to the tensile strength of materials, is a key parameter in plastic processing. In particular, the necessity of processes such as stamping makes high formability indispensable for materials. High formability generally requires a low yield ratio, which is equivalent to a high work hardening rate and resistance to deformation from yielding to plastic instability [1–3]. The lack of strain hardening with a high yield ratio results in inhomogeneous strain redistribution during stamping. On the other hand, the yield ratio is also an important index for component design to ensure structural safety, and a high yield ratio can

* Corresponding author at: School of Materials Science and Engineering, Northeastern University, Shenyang 110819, PR China.
E-mail address: zhaoxl@mail.neu.edu.cn (X. Zhao).

https://doi.org/10.1016/j.jallcom.2023.170024
0925-8388/

effectively save materials and reduce weight [4]. Therefore, various yield ratios are required for different applications.

In recent years, titanium alloys have been widely applied in aerospace and chemical fields for their high specific strength and excellent corrosion resistance [5]. It is known that titanium alloys can exhibit α, β and ω phases dependent on temperature and pressure [6,7]. In order to improve the mechanical strength of α or α + β titanium alloys, a number of efforts, including severe plastic deformation [8], addition of alloying elements [9] and thermo-mechanical treatment [10], have been attempted in the last three decades. However, achieving good strength-ductility balance in α or α + β titanium alloys is still challenging. Thus, studies on β and metastable β titanium alloys have attracted rich interest recently, particularly due to their high potential of excellent ductility and lower elastic moduli than those of α, and α + β alloys [11], which can effectively prevent the stress shielding caused by elastic modulus mismatch between materials and bones. Therefore, these alloys have also attracted widespread attention in the biomedical fields [12–14].

The yield ratio of a metastable β titanium alloy is closely related to its deformation mechanisms [15]. When the critical triggering stress of deformation-induced transformation/twinning is lower than the yield strength of the matrix, the stress−strain curve of the alloy will exhibit a typical “double-yielding” phenomenon [16,17]. In this case, the transformation/twinning is stress-induced, and the alloy has both low yield strength and high work hardening ability. Therefore, it is expected to achieve a large-scale regulation of the yield ratio and meet the service requirements under different working conditions by regulating the critical trigger stress of stress-induced phase transformation/twinning and improving the tensile strength by continuous phase transformation.

The critical trigger stress of the stress-induced martensitic phase transformation (SIMT) depends on various factors, such as solute concentration [18–20], grain sizes of the β phase [21,22], volume fractions of the second phase [23–27], deformation temperature [28,29] and strain rate [30,31]. Due to the metastable characteristics of metastable β titanium alloys, their microstructures, including phase constituents, size, morphology, and distribution, can be changed through low-cost thermal treatments. Furthermore, thermal treatment is more feasible for the components after processing. Therefore, thermal treatment is expected to become a low-cost and effective way to control the yield ratio of alloys.

The α and β duplex structure can be obtained by heat treatment in the α and β dual phase region. The effects of the α phase fraction on the deformation mechanism and mechanical properties have attracted great research attention. Liao et al. studied the metastable β-51.1Zr-40.2Ti-4.5Al-4.2 V (mass %) alloy with α and β dual phases and found that with increasing α phase fraction, {101(−)1}α′ deformation twinning and kink bands disappeared, and only the stress-induced α′ martensitic transformation occurred [32]. Frank Niessen et al. found that in the β-type Ti–10 V–2Fe–3Al alloy containing 5% α phase, the stress-induced α′′ martensite phase transformation and {130}< 310 > α′′ mechanical twinning occurred in the three-point bending test [33]. In a study of α and β dual-phase Ti–10 V–2Fe–3Al alloy, Li et al. also found that with an increase in the α phase fraction, the stress-induced α′′ martensitic transformation in the alloy became difficult. When the α phase fraction exceeded 50%, the stress-induced martensitic transformation was completely suppressed [25]. Chen et al. found that in the Ti–10 V–3Fe–3Al alloy, the deformation mechanism of the alloy changed from SIMT and stress-induced twinning (SIT) to dislocation slip with increasing α phase fraction [18,25]. The above results suggest that either the deformation-induced martensite transformation or the mechanical twinning operative in metastable β Ti alloys containing the mixed α and β phases are strongly affected by the volume fraction of the α phase.

The above research focuses on the deformation mechanism change in the β phase, but little evidence has shown that the β phase deforms initially. When two phases coexist, which phase deforms preferentially and how to coordinate the deformation between two phases is of great significance for understanding the microscopic deformation mechanism and crucial for adjusting the yield ratios of the materials. During the thermal treatment, the β phase stability will change due to the α-stabilizing and β-stabilizing elements partitioning between the phases, whereas whether neutral element (Zr or Sn) partitioning occurs is obscure.

As a solid solution strengthening element, Zr is infinitely soluable in titanium alloys. The high addition of Zr can prohibit hydroxyapatite formation for the removal implants and lower the magnetic susceptibility [34–36]. High Zr-containing titanium alloys have attracted attention in biomedical fields [18,37]. Ti-30Zr-5Mo is a metastable β titanium alloy with a low yield ratio and stress-induced α′ phase transformation designed for spinal fixation rods [18,38]. Whether the neutral Zr element will redistribute between the α and β phases, how it affects the β stability, which is closely related to the deformation mechanism and the work hardening ability of the alloy, and how the α phase affects the stress-induced α' phase transformation with the same crystal structure need to be clarified. Furthermore, the β domain is also affected by changing the α phase fraction. It may change the deformation mechanism and affect the work hardening behavior. In addition, due to the element partitioning, the α/β interfaces may change and have an effect on the work hardening ability. The aim of this work is to investigate the synergistic effects of β stability, β domain, and α/β interfaces on the regulation of the yield ratio of a Ti-30Zr-5Mo alloy containing mixed α and β phases.

2. Materials and methods

The specific preparation process of the Ti-30Zr-5Mo (mass %) material has been provided in our previous work [30]. The as-cast alloy was forged at 1000 °C and then air cooled. Small samples cut from the forged alloy were solution treated at 600, 650, 680 and 700 °C for 60 min followed by ice-water quenching. The β transus temperature is 690 °C, as determined by metallography. They are referred to as ST600, ST650, ST680, and ST700, respectively, and the processing procedure is shown in Fig. S1.

To evaluate the mechanical properties of the materials, dog-bone-shaped tensile specimens with a gauge length of 13 mm and a cross section of 3 mm × 1.5 mm were prepared by wire electrical discharge machining (WEDM) and mechanical polishing to #3000 grit by SiC papers. Tensile tests were performed at room temperature using a Shimadzu AG-Xplus100kN tensile testing machine with a rate of 0.5 mm/min. At least three specimens were tested for each condition to ensure validity.

The specimens for microstructure analysis were mechanically polished using #800~#3000 grit SiC papers followed by electropolishing with a solution of 5% perchloric acid, 35% n-butanol, and 60% methanol at 263 K to remove the residual deformation layer induced by mechanical polishing. The specimens for optical observation (Zeiss AXIO) were further etched with Kroll’s solution of 4% hydrofluoric acid, 10% nitric acid, and 86% deionized water. The in-situ microstructural evolution and ex-situ microstructure details were analyzed by scanning electron microscope (Zeiss Gemini 300) with electron backscatter diffraction (EBSD, Symmetry). EBSD analysis was carried out at an accelerating voltage of 20 kV and an acquisition rate of 383.64 Hz. The element distribution was analyzed by a transmission electron microscope (TEM, JEM-2100 F) equipped with an energy dispersive spectrometer (EDS), and the voltage was 200 kV. The specimens for TEM observation were initially mechanically thinned to around 60 μm and then electrolyzed with the same electropolishing solution at 238 K and with 35 V voltage. The

phase was identified by the X-ray powder diffraction method. The XRD (Smart Lab) tests were carried out using Cu-K_α radiation at an accelerating voltage of 40 kV, current of 30 mA, and scan range between 30° and 90°with a scan rate of 6°/min. The phase fraction was determined by XRD using the following equation:

$$V_i = \frac{\frac{1}{n}\sum_{j=1}^{n}\frac{I_i^j}{R_i^j}}{\frac{1}{n}\sum_{j=1}^{n}\frac{I_\beta^j}{R_\beta^j} + \frac{1}{n}\sum_{j=1}^{n}\frac{I_{\alpha'}^j}{R_{\alpha'}^j}} \quad (1)$$

V_i represents the volume fraction of the *i*-th phase, *I* is the diffraction peak intensity of each phase, *R* represents the reference specific intensity of each phase, and the expression is:

$$R_{hkl} = \left(\frac{1}{v^2}\right)\left|F\right|^2 P\left(\frac{1+cos^2 2\theta}{sin^2\theta cos\theta}\right)e^{-2M} \quad (2)$$

v is the unit cell volume, *F* is the structure factor of the unit cell, *P* is the multiplicity factor, θ is the Bragg diffraction angle, and e^{-2M} is the temperature factor.

The micromechanical properties of different phases were examined using a nanoindentation facility (Bruker Hysitron TI980) equipped with a scanning probe microscope (SPM), and more than 5 indentations were conducted at each phase to achieve statistically valid data. All measurements were conducted with a fixed depth of 50–80 nm.

3. Results

Fig. 1 shows the XRD patterns of various heat-treated materials. It is clear that ST700 is composed of a single β phase, while ST600, ST650, and ST680 consist of both α/α′ and β phases. With increasing temperature, the intensity of the α/α′ peak decreases, which is due to the continuous dissolution of the α/α′ phase. The volume fractions of the α/α′ phase in the ST600, ST650, ST680 and ST700 materials are 50%, 40%, 20% and 0%, respectively (Fig. 1(b)). Based on elements analysis shown later, this phase is α rather than α′, 50α, 40α, 20α and 0α are used hereinafter to refer to materials containing different α phases.

Fig. S2 shows the optical micrographs of the materials after forging and thermal treatments. It is clear that the widmanstatten and basket-weave microstructure can be observed in the forged material. After thermal treatments, a large number of fine acicular-like α or α′ phases with hexagonal closed packed structure exist inside the initial β grains. In the ST600 and ST650 materials, it is difficult to distinguish the details of the very fine phases under OM (Fig. S2(b-c)). However, in the ST680 material, the acicular second phases observed in the matrix decrease, but the size coarsens (Fig. S2(d)). When the temperature increases to 700 °C, as shown in Fig. S2(e), the material consists of a single equiaxed structure. Combined with the XRD patterns, it can be seen that the fine or coarse second phases in the matrix are the α or α′ phases, and the equiaxed phase is the β phase.

Fig. 2 shows the EBSD phase map of various materials with the β matrix in green and the α phase in red. For the 50α material, the colony α/α′ extends from the grain boundaries into the grain interiors of the β phase, and the acicular α/α′ phases are distributed inside the β phase. With increasing temperature, the colony and acicular α/α′ phase become shorter and thinner. When the temperature increases to 680 °C, both the number and size of the colony and acicular α phase significantly decrease. With increasing temperature, the area fraction of the α phase decreases from 29.9% in ST600 to 18.9% in ST650 and to 4.1% in ST680. The tendency is similar to that determined by XRD, although the data obtained by EBSD are lower than those calculated by XRD due to the limited recognition rate of EBSD mapping or the tiny α phase.

Fig. 3 shows the mechanical properties of the different materials. Their typical engineering stress–strain curves and the changes in strength and elongation are presented in Fig. 3(a) and (b), respectively. The yield strength (YS) and ultimate tensile strength (UTS) of the 50α and 40α materials are higher, and the materials yield continuously. With a decrease in the α phase content, the 20α and 0α materials exhibit a typical "double-yielding" phenomenon, and the YS and UTS decrease while their total elongations (tELs) increase significantly. As the α phase content in the materials decreases from 50% to 40%, the UTS and YS decrease from 1110 to 985 MPa and from 1013 to 944 MPa, respectively. Due to the “double-yielding” phenomenon, the YS of the 20α material is 531 MPa and decreases to 253 MPa as the α phase content decreases to 0%, and the UTS decreases from 926 MPa to 823 MPa. The uniform elongation (uEL) and tEL increase from 3.6% to 27.5% and from 10.1% to 34%, respectively, as the α phase content decreases from 50% to 0. The yield ratio decreases from 0.91 to 0.31 as the α phase content decreases from 50% to 0, although there is a fluctuation in the 40α material.

Numerous studies have shown that the "double-yielding" phenomenon of materials is related to the stress-induced phase transformation or mechanical twinning [39–41]. To reveal the relationship between the primary yielding phenomenon and the microstructure change, a loading–unloading test was performed for the 0α material. When the stress–strain curve entered the primary yielding region, the material was unloaded. The diffraction pattern

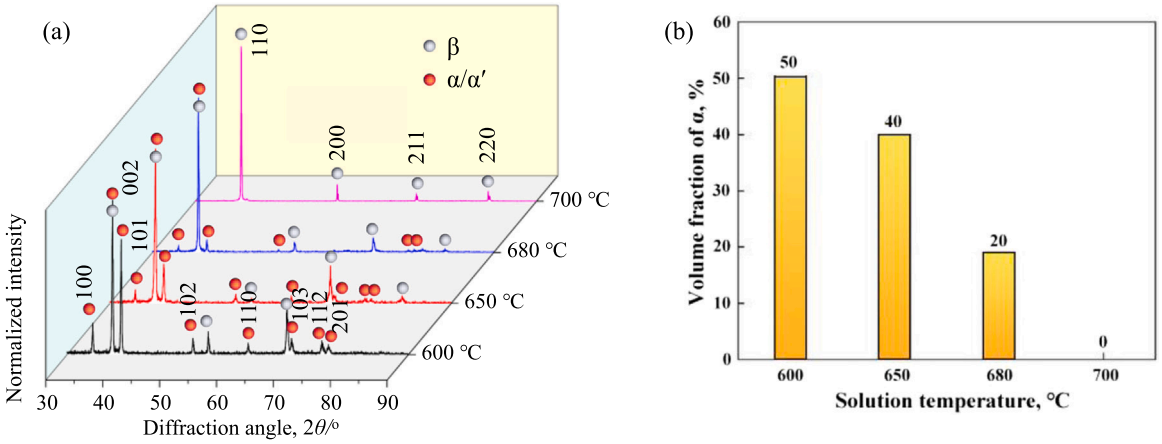

Fig. 1. (a) XRD patterns and (b) volume fraction of α phase in the Ti-30Zr-5Mo materials treated at different temperatures.

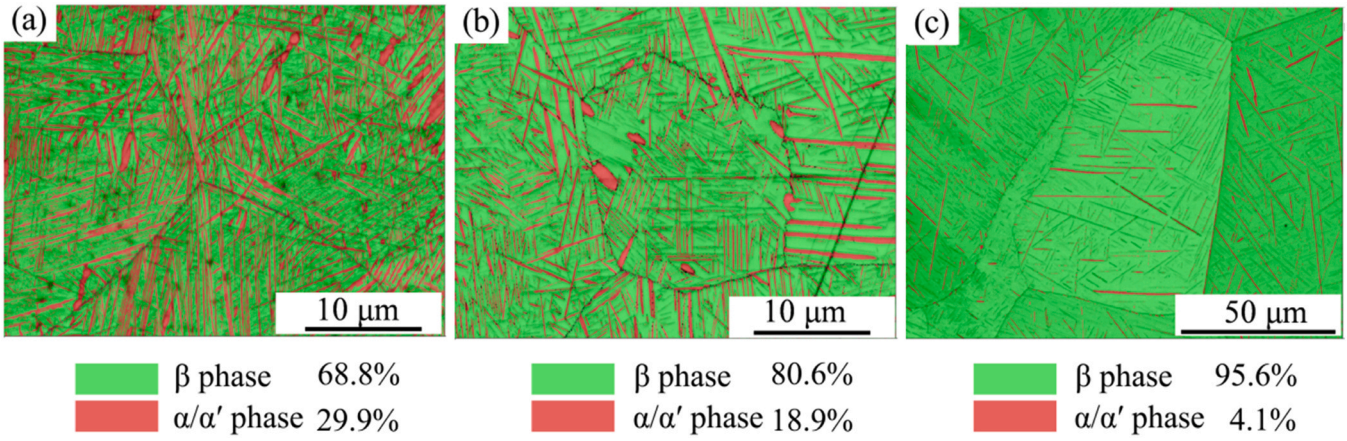

Fig. 2. Phase map showing phase distributions in different materials; (a) ST600 (50α), (b) ST650 (40α), and (c) ST680 (20α).

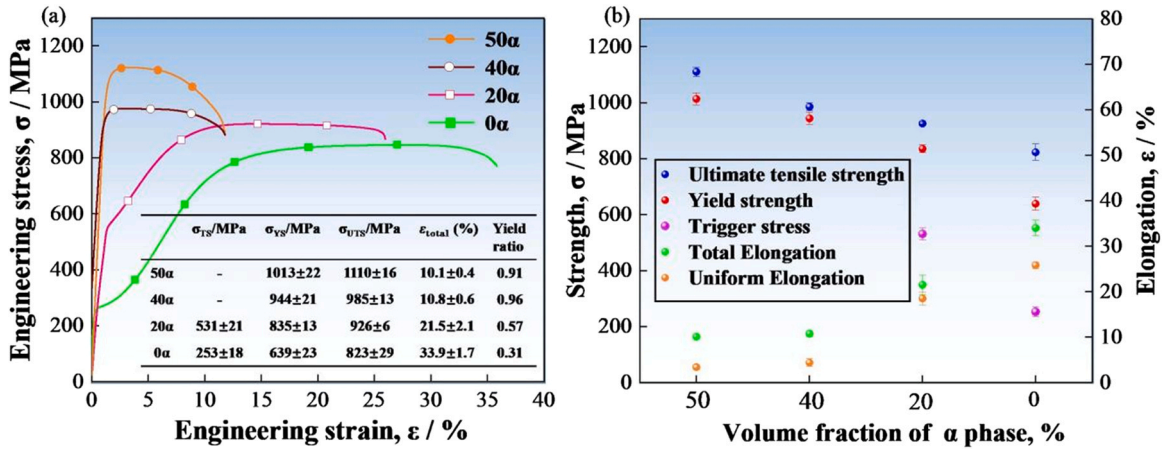

Fig. 3. Tensile properties of Ti-30Zr-5Mo alloy with various α volume fraction; (a) engineering stress-strain curves and mechanical properties with standard deviations, and (b) changes of strength and elongation with varying α phase fraction.

(Fig. S3 (a)) and acicular morphology (Fig. S3 (b)) of the α′ phase can be easily identified, verifying that the first yield strength corresponds to the critical trigger stress of the stress-induced α′ martensitic transformation.

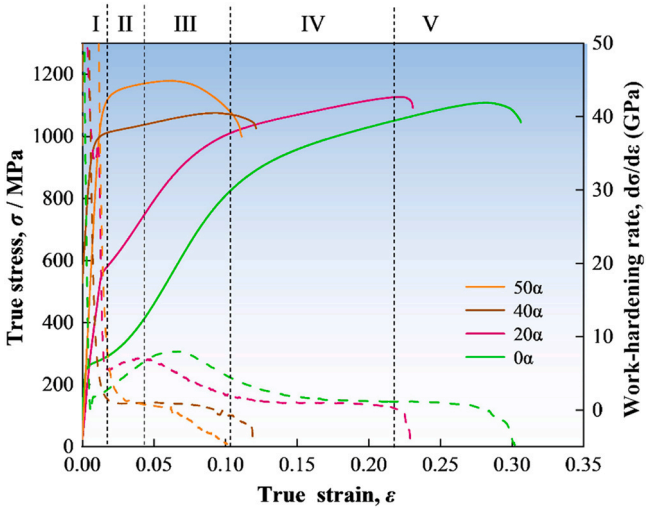

Fig. 4. True stress-strain curves (solid) and work hardening rate (dash) as a function of true strain for Ti-30Zr-5Mo alloy with various α volume fractions.

For high-performance structural materials, a sufficient strain hardening ability is required to prevent the early occurrence of necking. Fig. 4 shows the true stress–strain curves and the corresponding work-hardening rate (WHR) of the different materials. Similar to conventional alloys with SIMT or SIT phenomena, the work hardening of the 20α and 0α materials can be divided into five typical stages based on the slope change in the curves, i.e., dropping continuously (stage I), surging in a narrow plastic deformation range (stage II), plunging quickly (stage III), hitting a plateau (stage IV), and going down until fracture (stage V). Unlike the 20α and 0α materials, whose WHRs exhibit a “hump” shape, the WHR curves of the 40α and 50α materials only have three stages, i.e., decreasing continuously (stage I) to a plateau (stage II) and declining until fracture (stage III). Compared to the 50α material, the 40α material exhibits a longer plateau, indicating better necking resistance.

To elucidate the different work-hardening behaviors of different materials, the materials strained to fracture are examined by XRD, and the patterns are shown in Fig. 5. Since the α phase and α′ martensite phase have the same crystal structure and similar lattice parameters, the peaks in the patterns coincide. However, the content of stress-induced α' martensite can be determined by the peak height change of α/α' phase in the XRD pattern before and after deformation. For the 50α and 40α materials, the β phase with a body-centered cubic (BCC) structure is stable, and almost no phase transformation occurs, indicating that the plastic deformation of the β phase in these two materials is dominated by dislocation slip, in agreement with in many BCC-type titanium alloys [18,42,43]. Its

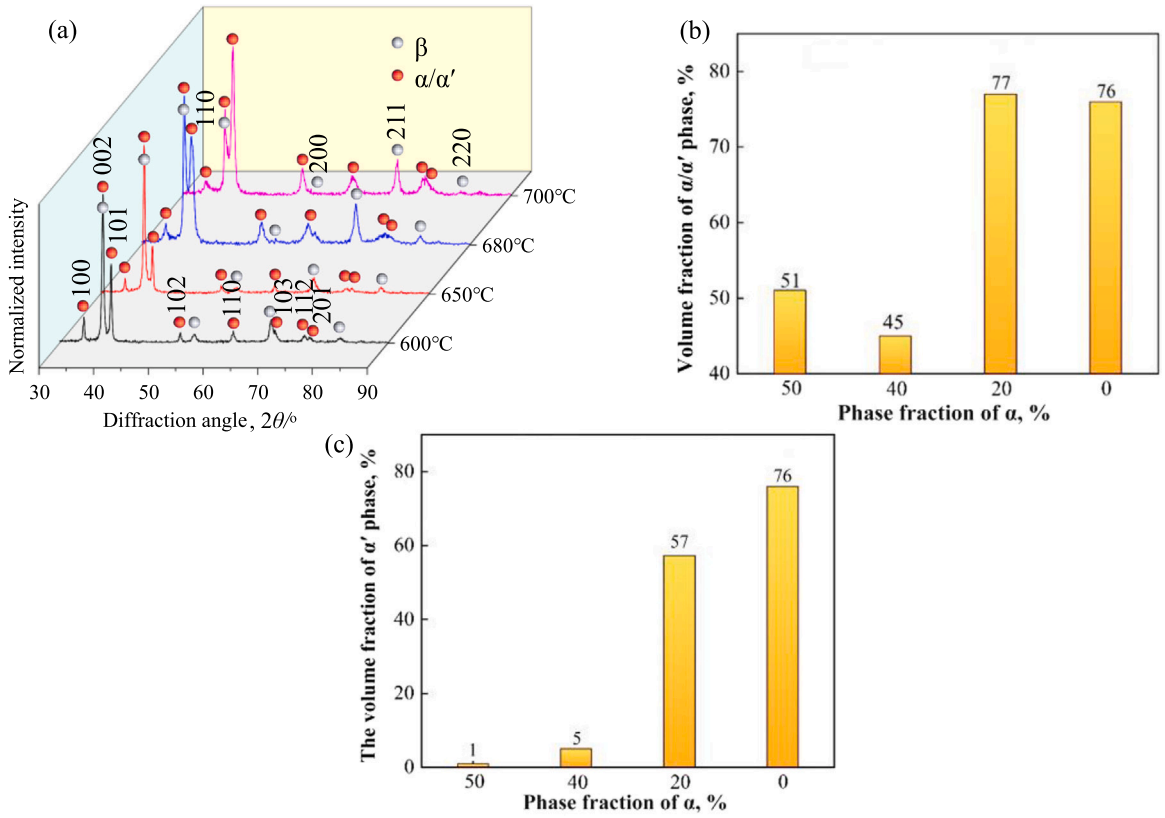

Fig. 5. (a) XRD spectra, (b) volume fraction of α/α′ phase, and (c) volume fraction of stress-induced α′ phase in the Ti-30Zr-5Mo materials with various α volume fraction after fracture.

limited ductility is related to the limited strain hardening ability, which results in the inhomogeneous deformation in the initial stage of deformation [44]. Unlike the 50α and 40α materials, whose volume fractions of the α/α' phase are almost unchanged (1% and 5%), it is evident that the stress-induced martensite transformation from β to α' occurs in the 20α and 0α materials during deformation. The good ductility is related to the SIMT. As indicated by the volume fraction change of the α/α' phase shown in Fig. 5(c), the amount of stress-induced martensite (SIM) α' phase is much larger in the 0α material (76%) than in the 20α material (57%), which provides better work-hardening abilities for the 0α material.

To investigate the details of the deformation modes in the materials with different WHR evolution tendencies, the deformation microstructures of the fractured 50α and 40α materials are analyzed by EBSD, as shown in Fig. 6. There are no apparent microstructure differences between the heat-treated and the fractured materials, i.e., The fractured materials are still composed of α and β phases. The staggered α laths are evenly distributed in the β matrix, and no obvious stress-induced α' martensite is observed. Compared to the kernel average misorientation (KAM) maps of the heat-treated material shown in Fig. 6(b) and (f), a larger misorientation is observed at the grain boundaries and α/β phase boundaries in the fractured 40α and 50α materials shown in Fig. 6(d) and (h), indicating a higher density of defects and a larger plastic deformation degree at those boundaries. Furthermore, the average value of KAM is larger in the 50α material (0.571) than in the 40α material (0.558).

The relationship between the α phase and stress-induced α′ martensitic transformation during deformation was investigated in the 20α material by in situ EBSD, as shown in Fig. 7. The strains (0%, 2%, 4% and 10%) are determined by both the stress–strain curve and the WHR curve in Fig. S4. They correspond to the initial strain of Stage I, Stage II, Stage III, and Stage IV, respectively.

The IPF maps of the 20α material at different strains are shown in Fig. 7. At a strain of 0%, the material is composed of α and β phases, and the acicular α phase is uniformly distributed in β grains. When the strain increases to 2%, the lath-like stress-induced α′ martensitic phases initiate from the β grain boundaries, cross the entire grain and stop at the other boundaries. It is confirmed again that the primary yield point in the stress–strain curve corresponds to the occurrence of stress-induced α' martensitic phase transformation. The α′ martensite can cross vertically when passing through the elongated α phase, which indicates that the α/β interfaces in this material are not strong enough to hinder the α′ growth. When the strain increases to 4%, the newly formed stress-induced α' martensite appears, and the preformed stress-induced α' martensite broadens significantly. When α' martensite with the same orientation meets during the broadening process merging will occur, indicating that the stress-induced α' martensite transformation will continue to occur in Stage II and that the preformed martensite broadens and consumes the β matrix in the material. The stress-induced α' martensite refines the β grains, leading to the dynamic Hall–Petch effect and continuously increased work hardening rates. When the strain increases to 10%, which corresponds to the end of Stage III, the stress-induced α' martensitic transformation is almost fully combined and occupies the entire grain. The stress-induced α' martensitic transformation is basically saturated, and the contribution of the stress-induced α' martensitic transformation to work hardening is balanced with the work softening caused by the reaction annihilation of dislocations. Compared with the fractured structures of the 20α material, no obvious broadened deformation products are found in the fractured structures of the 40α and 50α materials, again verifying that the stress-induced α' martensitic transformation is suppressed with increasing α content.

Fig. 8 shows the detailed analysis of the EBSD results for the 20α material strained at 2%. The orientation relationship between the

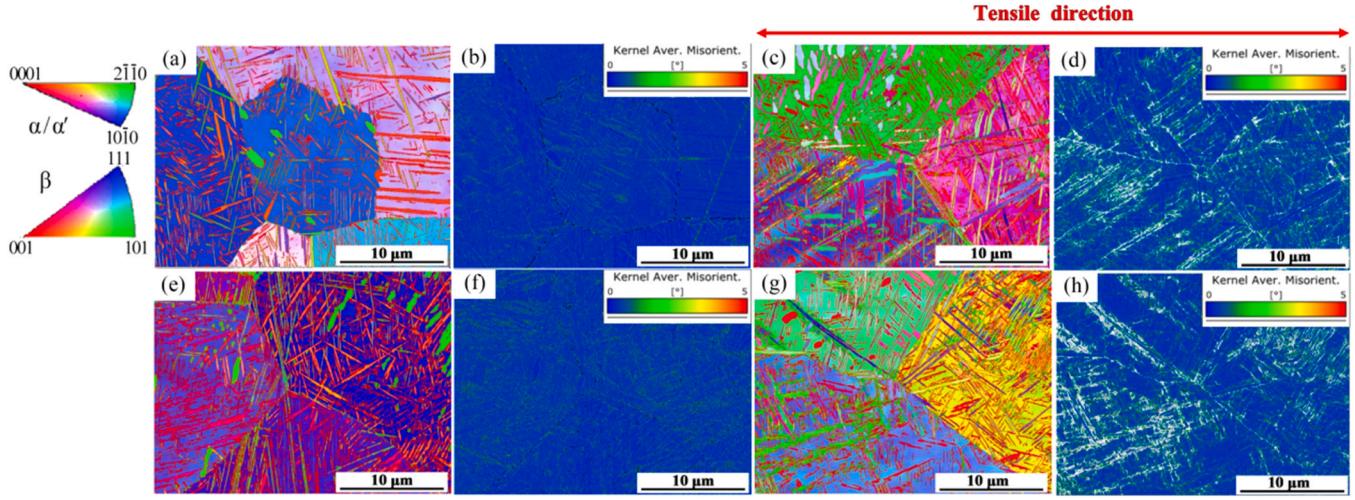

Fig. 6. (a), (b), (d) and (e) Inverse pole figure (IPF) and (c) and (f) KAM maps of the 40α and the 50α materials before and after deformation; (a) heat-treated 40α material, (b) and (c) fractured 40α material, (d) heat-treated 50α material, (e) and (f) fractured 50α material.

stress-induced α′ phase and the β matrix at the corresponding position of Fig. 8(a) is shown in Fig. 8(b). The Burgers orientation relationship $(0001)_{\alpha'}//(110)_{\beta}$, $< 112(-)0 >_{\alpha'}// < 111 >_{\beta}$ is followed between the α′ and β phases, which is the same as that between the quenched α′ and β phases [45]. The KAM map in Fig. 8(c) shows that a larger misorientation occurs at the α′/β and α′/α boundaries, indicating serious dislocation pile-up. In addition, the local strain gradient can be found in the stress-induced α′ phase, as the misorientation changes from high to low from the α′/β phase boundary to the interior of the α′ phase, and dislocations tend to pile up at the phase boundaries. Fig. 8(d)-(f) shows that the typical misorientation between α′ and α is 60°/ < 112(−)0 > , which corresponds to high-angle grain boundaries of type II [46,47]. When the stress-induced α′ meets the α phase, the α phase tilts a small angle of 4–7° around < 78(−)13(−) > to coordinate the deformation. The α phase is so narrow that the stress can be transferred from one boundary to the other; therefore, on the other side of the α phase boundaries, α′ with the same variant can nucleate and grow further. The α phase can hardly hinder the growth of the α′ phase.

To study the relationship between the α phase and stress-induced α' martensite phase transformation, the variant relationship between them during deformation was analyzed. Table 1 lists 12 possible variants for the β→α′ transformation in the studied titanium alloys through the Burgers orientation. Fig. 9(a) shows the 3D crystal orientation analysis of different variants in the labeled area of grain 1, and four variants of the α phase are observed in the region (V1-V4). When the strain increases to 2% (Fig. 9(b)), two variants of the stress-induced α' martensite (V1-α′ and V2-α′) appear. When the strain increases to 4% (Fig. 9(c)), the third variant (V3-α′) is activated. As the strain continues to increase (Fig. 9(d)), α′ martensitic variant 3

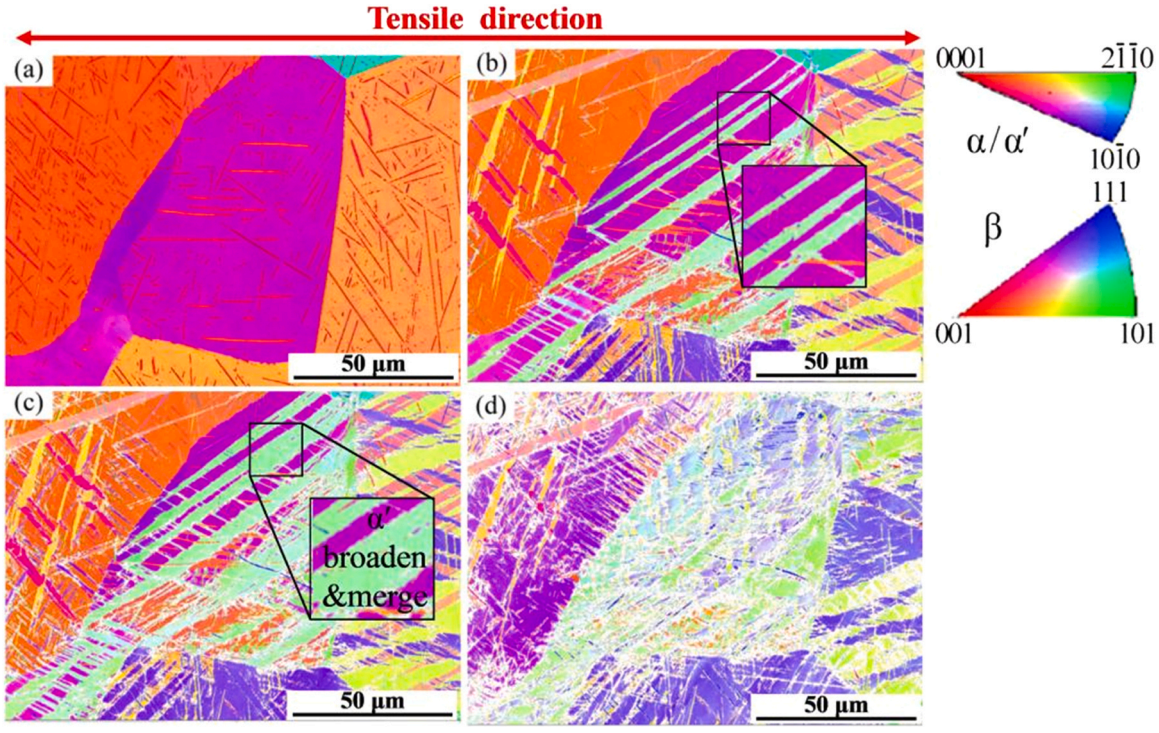

Fig. 7. IPF maps of the 20α material at different strains during in-situ EBSD analysis; (a) ε = 0%, (b) ε = 2%, (c) ε = 4% and (d) ε = 10%.

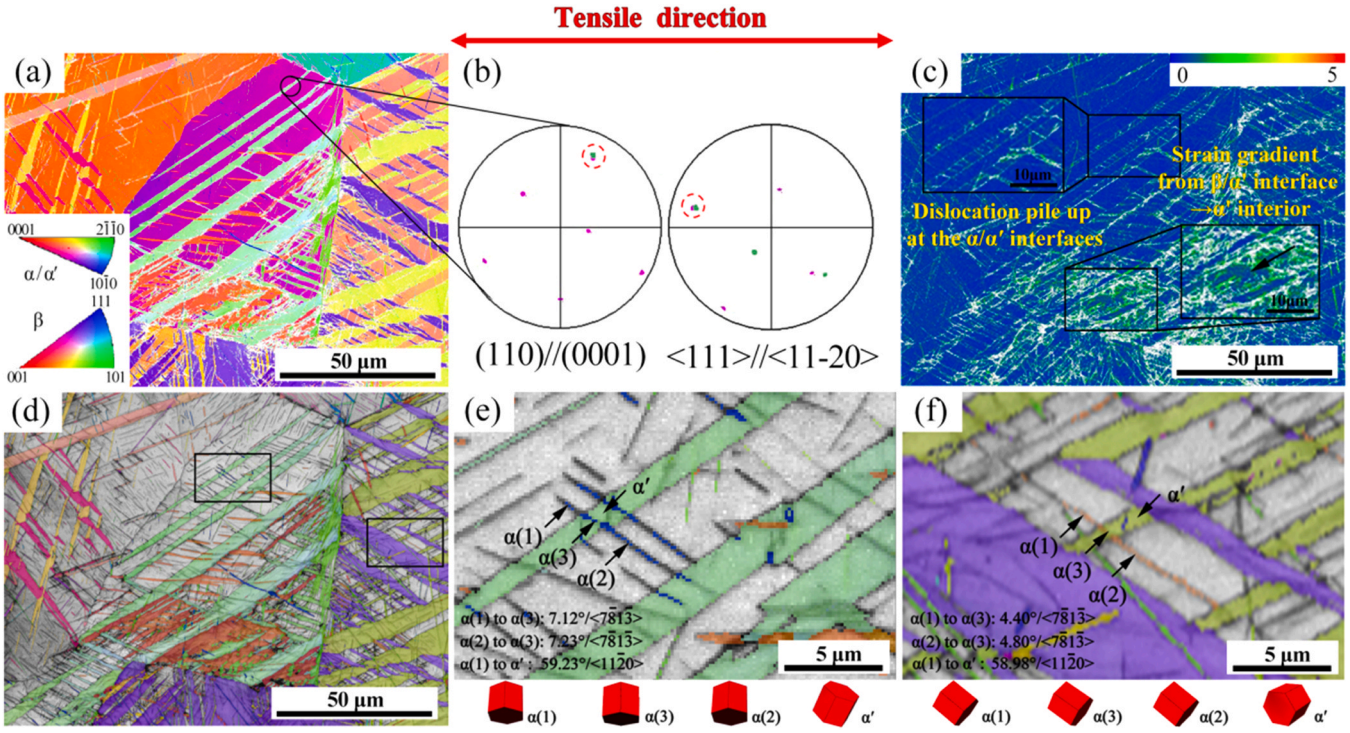

Fig. 8. EBSD analysis of the 20α material strained at 2%; (a) IPF map, (b) overlap of pole figures of two phases in annotation area in (a), (c) KAM map, (d) The IPF and BC map of α /α′ phase, and (e) (f) Misorientation between α and α′ phases.

Table 1
Possible 12 variants of β→α/α' phase transformation in the studied titanium alloy based on Burgers orientation relationship.

α/α' variants	$\{110\}_\beta$ // $\{0001\}_{\alpha/\alpha'}$	$<111>_\beta$ // $<11\bar{2}0>_{\alpha/\alpha'}$	α/α' variants	$\{110\}_\beta$ // $\{0001\}_{\alpha/\alpha'}$	$<111>_\beta$ // $<11\bar{2}0>_{\alpha/\alpha'}$
V1	$(011)_\beta$ // $(0001)_{\alpha/\alpha'}$	$[11\bar{1}]_\beta$ //$[11\bar{2}0]_{\alpha/\alpha'}$	V7	$(101)_\beta$ // $(0001)_{\alpha/\alpha'}$	$[\bar{1}11]_\beta$ //$[11\bar{2}0]_{\alpha/\alpha'}$
V2		$[1\bar{1}1]_\beta$ //$[11\bar{2}0]_{\alpha/\alpha'}$	V8		$[11\bar{1}]_\beta$ //$[11\bar{2}0]_{\alpha/\alpha'}$
V3	$(10\bar{1})_\beta$ // $(0001)_{\alpha/\alpha'}$	$[1\bar{1}1]_\beta$ //$[11\bar{2}0]_{\alpha/\alpha'}$	V9	$(1\bar{1}0)_\beta$ // $(0001)_{\alpha/\alpha'}$	$[11\bar{1}]_\beta$ //$[11\bar{2}0]_{\alpha/\alpha'}$
V4		$[111]_\beta$ //$[11\bar{2}0]_{\alpha/\alpha'}$	V10		$[111]_\beta$ //$[11\bar{2}0]_{\alpha/\alpha'}$
V5	$(01\bar{1})_\beta$ // $(0001)_{\alpha/\alpha'}$	$[\bar{1}11]_\beta$ //$[11\bar{2}0]_{\alpha/\alpha'}$	V11	$(110)_\beta$ // $(0001)_{\alpha/\alpha'}$	$[1\bar{1}1]_\beta$ //$[11\bar{2}0]_{\alpha/\alpha'}$
V6		$[111]_\beta$ //$[11\bar{2}0]_{\alpha/\alpha'}$	V12		$[\bar{1}11]_\beta$ //$[11\bar{2}0]_{\alpha/\alpha'}$

(V3-α′) broadens, and when the strain increases to 10%, variant 3 (V3-α′) occupies most of the grain 1 region. The preactivated variant 1 of α′ martensitic (V1-α′) disappears completely, and only a small amount of variant 2 of (V2-α′) is visible, indicating that V1-α′ and V2-α′ undergo reorientation to the same orientation as variant 3 (V3-α′) with increasing strain. The broadening and reorientation of martensite will affect the mechanical properties of the materials. On the one hand, the phase boundaries (PBs) (α′/β and α/β) are effective obstacles to dislocation motion, the size of the α′ martensitic plates formed in the early stage of deformation is small, and high densities of α′/β and α/β interfaces exist, resulting in an increase in strain hardening. However, as the strain increase, the β→α′ phase transformation continues to occur, along with the reorientation and merging of the pregenerated α′ phase, reducing the interface area and gradually weakening the strain hardening effect. On the other hand, reorientation can effectively alleviate the stress concentration.

Fig. 10 shows the fractography of the 50α, 40α, 20α and 0α materials. The dimples in both the 50α and 40α materials are large, while compared to the 40α material with uniform dimples, some shallow dimples are visible in the 50α material. In contrast, the dimples in the 0α material are smaller and evenly distributed, while in the 20α material, mixed dimples with the similar morphologies in the 40α and 0α materials are observed. Combined with Fig. 8, numerous stress-induced α′ martensitic phase transformations occur during tensile deformation in the 20α and 0α materials, and the content reaches 57% and 76%, respectively. It is speculated that the fine dimples in the fracture of the 20α material are caused by stress-induced α′ martensite, while the large dimples are related to the α phase, and the verification will be carried out in the future. The SIMT during tensile deformation guarantees excellent tensile plasticity of the materials with low α phase content.

4. Discussion

4.1. Regulation of α phase content

Static recrystallization and α→β phase transformation occur in the forged material when subsequently heated below the β transus temperature, and the α phase is retained by dissolving the α phase formed during air cooling after forging [48]. During the transformation process of α→β, the β phase nucleates at the α/β interfaces and then grows. In the initial stage, the concentration of β stabilizing elements in the α phase is very high due to the limited content of the β phase, resulting in an obvious element concentration difference

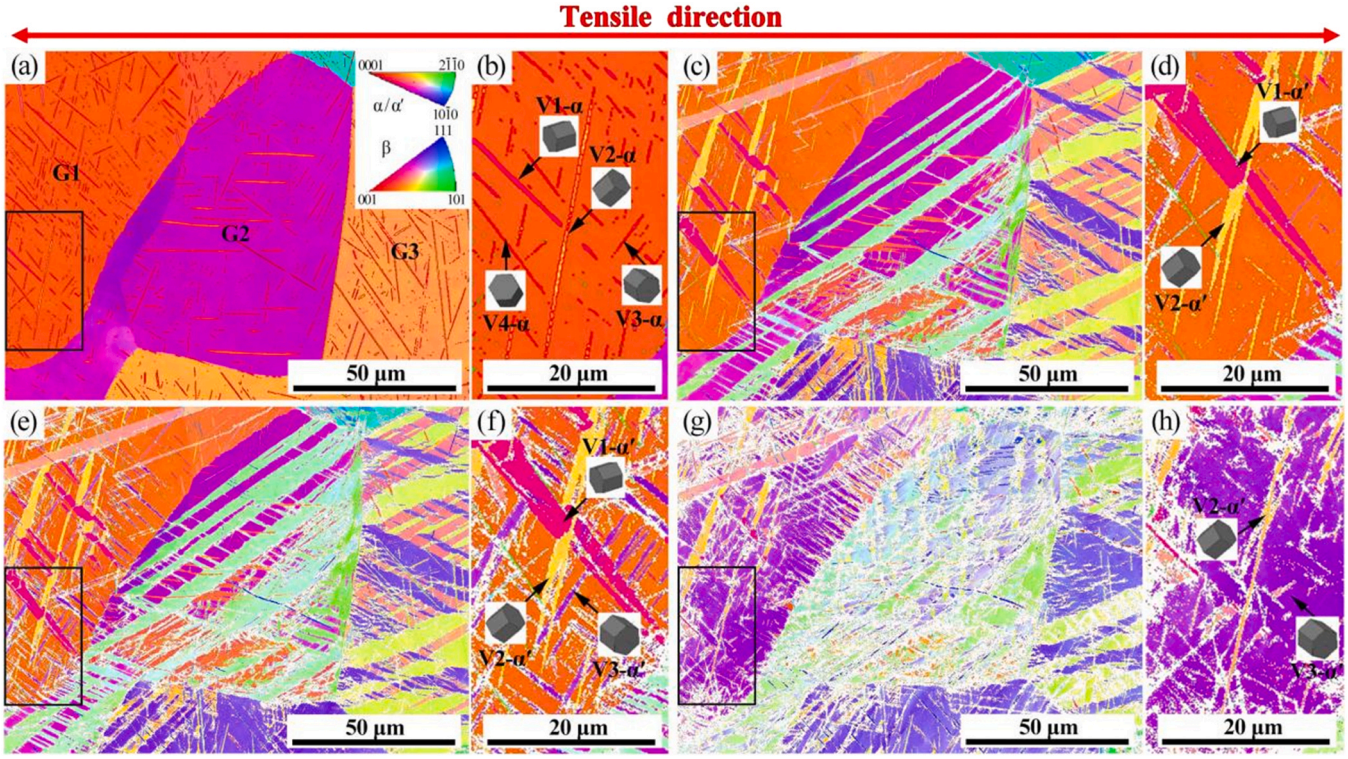

Fig. 9. IPF maps of the 20α material at different strains; (a) ε = 0%, (b) ε = 2%, (c) ε = 4% and (d) ε = 10%.

between these two phases. Therefore, the dissolution rate of the α phase at the interface is fast, and the α/β phase boundaries are changed to ellipsoidal or acicular-like shapes [49]. Due to the different thermal stabilities of the α and β phases, with increasing temperature, the α phase formed during the forging process gradually changes to the β phase, and finally different contents of the acicular α phase can be obtained. The materials are kept at a certain temperature for 60 min, which is long enough for the element diffusion in each phase to reach the equilibrium state at that temperature.

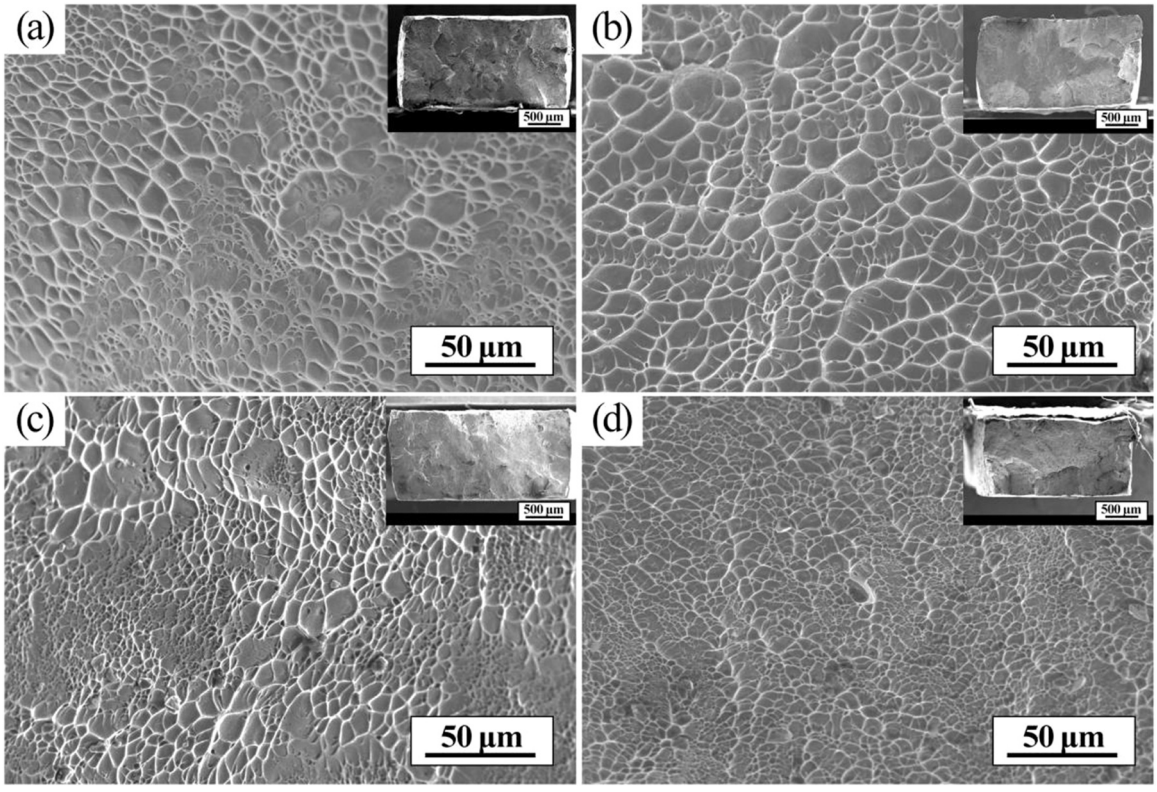

Fig. 10. SEM fractographs of the Ti-30Zr-5Mo alloy with various α volume fractions; (a) 50α, (b) 40α, (c) 20α and (d) 0α.

4.2. Effect of the α phase fraction on the deformation mechanism

For the dulex phase titanium, which phase deforms initially is crucial to understand the deformation mechanism. The micromechanical properties of the α and β phases are determined by nanoindentation. Table 3 summarizes the elastic modulus (E_r) and nanohardness (H) of the α and β phases in the 50α and 20α materials. Compared with the β phase, the hardness of the α phase is more scattered, which is caused by anisotropy in the α phase with a dense hexagonal structure [50–53]. In addition, the hardness of the α phase is higher than that of the β phase, and as the α phase content increases, the hardness difference between the β and α phases becomes larger. In the 50α material, the hardness of the β phase and α phase are 2.6 GPa and 3.8 GPa, respectively. In the 20α material, the hardness of the β phase and α phase are 3.2 GPa and 3.8 GPa, respectively. Similarly, the elastic modulus of the α phase is greater than that of the β phase, and with increasing α phase content, the elastic modulus difference between the two phases becomes larger. Therefore, deformation will initiate from the β phase, and the deformation mechanism of the β phase becomes important.

The above results indicate that the deformation mechanism of the alloy changes with varying α phase fractions. The stress-induced α′ martensite phase transformation occurs during deformation in the 0α and 20α materials. As the content of the α phase increases to or over 40%, the stress-induced α′ martensite transformation is hindered, suggesting that dislocation slip dominates during deformation.

It has been reported that the α phase content affects the deformation mechanism by tuning the β domain size and β stability through element partitioning in the α and β phases. Liao [32] et al. showed that in a metastable Ti-Zr-Al-V alloys, as the α phase content increases, V is enriched in the β matrix, and the β domain decreases, thereby changing the deformation mechanism of the alloy. Li [25] et al. said that in addition to the content, the morphology of the α phase was also important. The acicular and spherical α phases have the same effect on element partitioning but different effects on the β domain. The acicular α phase is more effective in reducing the β domains compared to the spherical phase.

For the Ti-30Zr-5Mo alloy, an acicular α phase is obtained to reduce the β domains for the mean free path of dislocations. As the α fraction increases to 40%, the combination of β domain refinement and β stability enhancement hinders the stress-induced α′ phase transformation. When the α phase content is 20%, the reduction in β domains is not evident due to the small amount of α phase, and the β phase stability change caused by element partitioning is more dominant. At high temperature, the β stabilizing element is prone to diffuse to the β phase, resulting in enrichment in the β phase, thereby increasing the β stability, and finally restricting the occurrence of stress-induced phase transformation.

To investigate the distribution of the β stabilizing element Mo and neutral element Zr in the α and β phases of materials with different α phase contents, TEM spectroscopy was performed. As shown in Fig. 11 and Table 2, Ti is evenly distributed in both the α and β phases of the 50α materials but slightly enriched in the α phase of the 40α and 20α materials. Mo, as a β stabilizing element is obviously enriched in the β phase. It is noteworthy that Zr is enriched in the β phase of all the studied duplex phase materials, which confirms that when Zr and the β stabilizing element coexist, Zr will be enriched in the β phase as a β stabilizing rather than a neutral element. Namely, in high-Zr-containing Ti alloys, the effect of Zr on the β stability is not negligible.

Fig. 12 is the *Bo-Md* value of high Zr-containing Ti-Zr-Mo and Ti-Zr-Nb alloys [38,54,55], it can be found that both the metastable β phase boundaries of the Ti-Zr-Mo and Ti-Zr-Nb alloys shift to the lower right corner and expand the β phase region, which indicates that Zr acts as a β stabilizing element in the high- Zr-containing alloys. The metastable β boundaries of Ti-Zr-Mo alloys are at the bottom right of Ti-Nb-Zr alloys, indicating that the β stabilizing ability of Zr in Ti-Zr-Mo alloys is greater than that in Ti-Nb-Zr alloys. Due to the stronger β stabilizing ability of Mo than Nb, it is inferred that the β stabilizing ability of Zr depends on the coexisting β stabilizing elements.

Mo_{eq} is an indicator to describe the β stability. In previous studies, Zr was treated as a neutral element and did not appear in the calculations, but as mentioned above, Zr exhibits β stabilizing ability, therefore, the calculation equation should be optimized. It has been reported that the β phase in the Ti-Mo and Zr-Mo binary alloys can be stabilized when the Mo content exceeds 10% and 3%, respectively [56,57]. For a simple calculation, in Ti-30Zr-Mo ternary alloys, a 7.9% content of Mo is required to stabilize the alloy; however, a single β phase is obtained in the Ti-30Zr-5Mo alloy, so the β stabilization effect of 30% Zr is equivalent to that of 2.9% Mo, so the optimized coefficient of Zr elements is calculated as 0.1, and the Mo_{eq} calculation is rewritten as.

$$Mo_{eq}= 1.0Mo+ 0.30Sn+ 0.33\ Nb+ 0.25Ta+ 0.10Zr+v.s.(mass\%) \quad (3)$$

As shown in Table 2, the β stability increases with increasing α phase fraction. Generally, when the Mo_{eq} is between 7.4 and 12, the stress-induced martensite phase transformation occurs; when the Mo_{eq} is between 13 and 18, deformation of the β-type titanium alloy is dominated by {332} < 113 > mechanical twinning. When the Mo_{eq} is above 20, dislocation slip becomes prominent [20]. The Mo_{eq} values of the β phase in the 40α and 50α materials are 11.96 and 13.34, respectively, which are located in a region where stress-induced martensitic phase transformation and mechanical twinning may occur. However, either SIM or SIT is observed in the 40α and 50α materials, which may be affected by the reduced β domains.

If the stress-induced α′ martensitic phase transformation occurs, what role does the α phase play in the α′ growth process? The stress-induced α′ martensitic phase in the 20α material can pass through the α phase, and the in situ EBSD analysis indicates that a large strain accumulates near the α′/α interfaces. It is deduced that the growth of the stress-induced α′ martensite phase is blocked by the α phase, and the strain accumulates at the α′/α interfaces. Then, the α will tilt a small angle to coordinate the deformation. Due to the small width of the α phase, the stress could be transferred from one boundary to the other. On the opposite interface of this α phase, the α′ martensite, which has the same variants as the preforming martensite will nucleate and continue to grow. The hardness difference between the α and β phases is not strong enough to hinder the growth of the α′ phase.

4.3. Effect of α phase content on the tensile properties

The yield ratio is dependent on both the YS and UTS. In metastable β alloys, the YS is the competitive result of SIM, SIT and dislocation slip. Commonly, the SIM and SIT trigger stress is dependent on the loading temperature, the chemical composition, the microstructure and the strain rate. In this study, the experiments are carried out at ambient temperature with the same strain rates, and the β phase deforms initially. Therefore, the microstructure and the chemical composition of the β phase are the main factors to consider. It is known that SIM trigger stress at room temperature is closely related to the martensite starting temperature (M_s); the smaller the difference between room temperature and M_s is, the lower the trigger stress of SIM. With increasing β stability, the M_s will be lowered, which results in the higher trigger stress of SIM and high yield ratio. Therefore, to obtain a low yield ratio, the β stability should be regulated. In the 0α and 20α materials, the SIM trigger stress is lower than the critical stress for dislocation slip; therefore, a lower yield strength is obtained in these two alloys. However, compared with the 0α material, the β phase stability in the 20α material is higher, resulting in a lower M_s, thereby leading to an

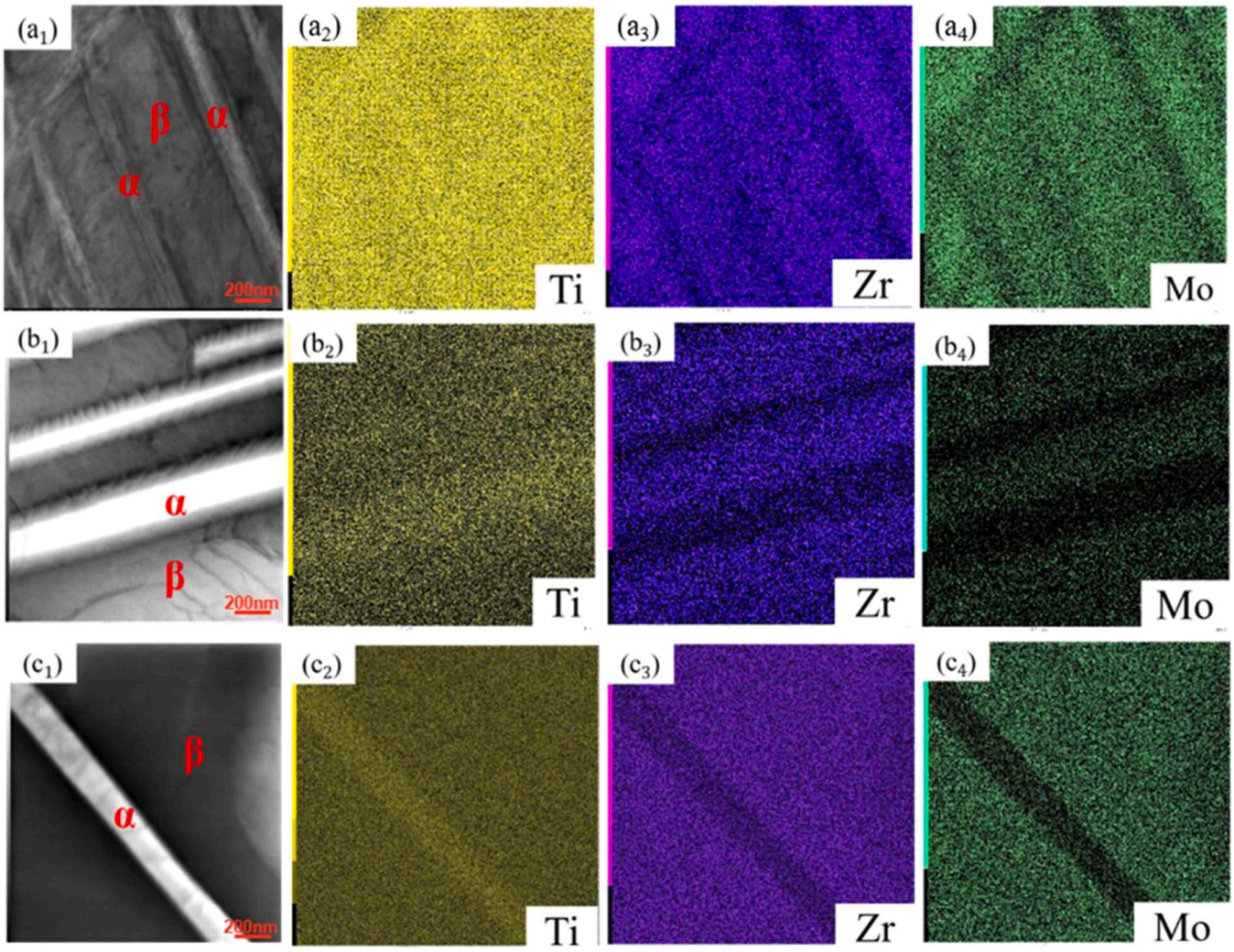

Fig. 11. TEM-EDS analysis of the Ti-30Zr-5Mo materials with various α volume fractions; (a_1-a_4) 50α, (b_1-b_4) 40α and (c_1-c_3) 20α.

Table 2
Chemical contents in β phase of the Ti-30Zr-5Mo materials with various α volume fractions.

Materials	Zr	Mo	Ti	Mo_{eq}
50α	35.4 ± 1.2	9.8 ± 0.4	Bal.	13.34
40α	37.8 ± 1.1	8.2 ± 0.9	Bal.	11.96
20α	37.8 ± 0.2	7.1 ± 0.2	Bal.	10.57
0α	28.9 ± 0.4	4.9 ± 0.5	Bal.	7.82

Table 3
Nano-indentation hardness of the Ti-30Zr-5Mo materials with various α volume fractions.

Materials	Phases	Elastic modulus/GPa	Micro hardness/GPa
50α	β	92 ± 9	2.6 ± 0.5
	α	115 ± 12	3.8 ± 0.7
20α	β	92 ± 2	3.2 ± 0.3
	α	103 ± 27	3.8 ± 1.9

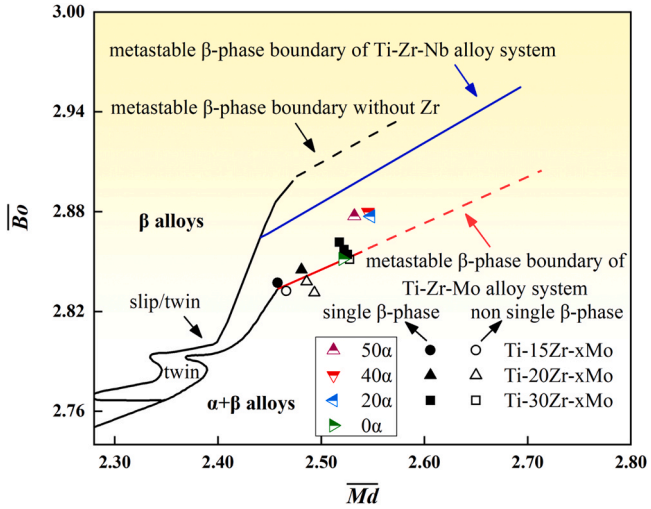

Fig. 12. Phase diagram for Ti alloys based on the $\overline{Bo}$ and $\overline{Md}$ as well as the deduced metastable β phase boundaries of high-Zr-containing Ti alloys.

increase in trigger stress at room temperature accordingly. In the 40α and 50α materials, the combination of a reduced β domain and high β stability hinders the SIM. The high β stability may lead to a much lower M_s, making the deformation temperature for SIM (M_d) near or lower than room temperature. SIM is prevented or the trigger stress of SIM exceeds the critical stress for dislocation slip; therefore, high yield strengths are obtained. It is noteworthy that even though both the 40α and 50α materials deform by dislocation slip, the 50α material has higher strength than the 40α material.

In Ti-30Zr-5Mo materials with various α phase contents, the acicular-like α phase is dispersed in the β matrix, the softer β phase

will be preferentially deformed during the deformation process, and the α/β phase interfaces as well as the grain boundaries provide barriers for dislocation slip. The Hall–Petch relationship is also obeyed in phase boundaries conditions. It has been reported that the Hall–Petch slope k_y is strongly dependent on the hardness ratio of the constituent phases. Increasing the hardness difference of the two phase dramatically increases the slope k_y and therefore renders a more effective barrier to dislocation motion [58]. Furthermore, the yield strength (σ_{YS}) of α + β dual-phase Ti alloys can be expressed as follows based on the rule of mixture:

$$\sigma_{YS} = (1 - f_\alpha)(\sigma_0^\beta + \sigma_{ss}^\beta) + f_\alpha\left((\sigma_0^\alpha + \sigma_{ss}^\alpha) + \sigma_{gb} + \sigma_{cs} + \sigma_{ms}\right. \quad (4)$$

when considering the strengthening effects of α and β phase by solid solution (includingσ_{ss}^α and σ_{ss}^β), grain boundaries (σ_{gb}), phase boundaries (σ_{cs}) and modulus mismatch (σ_{ms}) [59]. Therefore, the modulus mismatch between the β and α phases also hinders dislocation motion, thereby increasing the strength, similar to the mechanism of modulus hardening in the deformed particles. In the 20α material, the β phase is still metastable for SIM, the β phase transforms into the α′ phase under stress, and the α/β interfaces are not strong enough to hinder the α′ growth due to the minor hardness difference and modulus mismatch of 0.6 GPa and 11 GPa between the α and β phases. The α′ will continue to nucleate and grow on the other side of the α boundaries. In the 50α material, the main deformation is dislocation slip. The deformation also initially occurs in the β phase due to the lower hardness. Because the hardness difference and modulus mismatch of the α and β phases are much larger than that in the 20α material, the α/β interfaces are effective obstacles for the dislocations to go across, which can accumulate more geometrically necessary dislocations. In addition, the higher density of α/β interfaces in the 50α material renders more uniform deformation rather than stress concentration, causing a good combination of strength and ductility in the 50α material. From the interface strength of the 20α and 50α materials, it is speculated that the α/β interface strength of the 40α material is between those of the 20α and 50α materials. Therefore, the 40α material has a lower ultimate tensile strength than the 50α material. According to the Hall–Petch relationship, the lower yield strength of the 40α material is attributed to the β domains being larger than those of the 50α material. In addition to lowering the yield strength, SIM can coordinate the deformation and alleviate the stress concentration by extending from the high strain part to the low strain part, thereby delaying the necking of the materials and improving the ductility of the 0α and 20α materials [60]. For the dislocation slip-dominated 40α and 50α materials, the accommodation capacity of dislocations is mainly dependent on the α/β interfaces. The short dislocation free motion path lowers the pile-up degree, which makes $\gamma = \rho vb$ valid at strains up to 10%.

WHR is also an important parameter for the yield ratio because it can delay the necking of the material. The WHR curves of the 0α and 20α materials indicate that the SIM significantly improved the WHR. The “hump” is closely related to the SIM process. The WHR curve enters the second stage when SIM initiates. With increasing strain, the transformation from β to α′ continues, the preformed one grows and broadens, and the dislocation free motion paths decrease in the β matrix, causing the dynamic Hall–Petch effect. As the deformation proceeds, the WHR saturates, and then the reorientation of the α′ phase and annihilation of the dislocations lower the WHR, but due to the dynamic Hall–Petch effect, a WHR plateau can be obtained. Compared with the 20α material which has a smaller amount of α′ phase transformation, the plateau in the 0α material is longer. The SIM is beneficial for lowering the yield ratio while improving the ductility. For the 40α and 50α materials, the “humps” are invisible; however, working hardening still remains. Compared with the 50α material, the work hardening curve of the 40α material lasts longer. Therefore, it is speculated that due to the greater hardness difference of α/β interfaces in the 50α material, the obstruction effect of the interfaces on dislocations is stronger, and it is more likely to cause stress concentration to make the material neck earlier.

5. Conclusions

In this work, the α phase fractions of the Ti-30Zr-5Mo alloy were regulated by changing the heat treatment temperature parameters in the α + β dual phase field. The effects of the α phase content on the deformation mechanisms, yield strength and yield ratio of the alloy are then explored. The following conclusions are obtained.

(1) Acicular α phase evenly distributed in the matrix with different fractions can be obtained by changing the heat treatment temperature near or below the β transus temperature. Materials with α phase fractions of 50%, 40%, 20% and 0% are successfully prepared by annealing at temperatures of 600, 650, 680 and 700 °C for 60 min, respectively.
(2) The stress-induced α′ martensitic phase transformation occurs in the 0α and 20α materials during tensile deformation. The "double-yielding" phenomena appear in the stress–strain curves, and the yield ratios are 0.31 and 0.57, respectively. As the α fraction increases from 0% to 20%, the yield strength increases from 254 MPa to 531 MPa. The SIM is hindered in the 40α and 50α materials, and the yield strengths are increased to 944 MPa and 1013 MPa, respectively, owing to the second phase strengthening of the α phase. Correspondingly, the yield ratio reaches 0.96 and 0.91, respectively.
(3) In the Ti-30Zr-5Mo alloy with dual phases, the hardness of the α phase is higher than that of the β matrix, and the hardness difference between the α and β phases increases with increasing α phase content. Deformation initiates in the β phase of both single-phase and duplex-phase alloys. The deformation mechanism of the β phase is dependent on both the β domain and β stability. With increasing α phase content, the β domains are refined, while the β stability increases and the stress-induced α′ martensitic phase transformation is prevented. The α/β phase interfaces are the effective obstacles to hinder the dislocation movement, and the obstruction effect is more significant with increasing hardness difference between the α and β phases.
(4) When the α phase content is zero, the yield strength of the material is 254 MPa, the tensile strength is 843 MPa, and the total elongation is 34%. With the increase in the α phase, the yield strength and tensile strength increase with some ductility sacrifice. When the α phase content is 50%, the yield strength and tensile strength of the material reach 1013 MPa and 1110 MPa, respectively, and an excellent elongation of 10% remains. By changing the α phase fractions with low-cost thermal treatments, a large range of yield ratios from 0.31 to 0.96 and yield strengths from 254 to 1013 MPa can be obtained in the Ti-30Zr-5Mo alloy with decent elongations.

CRediT authorship contribution statement

Xiaoli Zhao: Writing, Investigation, Supervision, Funding acquisition. **Rongxin Zhu**: Investigation, Methodology. **Wenke Song:** Investigation, Methodology. **Lei Meng**: Investigation. **Mitsuo Niinomi**: Validation, Writing – review & editing. **Takayuki Nakano**: Validation, Writing – review & editing. **Nan Jia**: Validation, Writing – review & editing. **Deliang Zhang**: Validation, Writing – review & editing.

Data availability

Data will be made available on request.

Declaration of Competing Interest

The authors declare that they have no known competing financial interests or personal relationships that could have appeared to influence the work reported in this paper.

Acknowledgments

This work was financially supported by the National Natural Science Foundation of China (Nos. 52071068, 51922026), the Major Special Projects of the Plan "Science and Technology Innovation 2025" of China (No. 2020Z060), the Fundamental Research Funds for the Central Universities (Grant No. N2102013), the 111 Project, China (B16009) and JST-CREST (No. JPMJCR2194).

Appendix A. Supplementary material

Supplementary data associated with this article can be found in the online version at doi:10.1016/j.jallcom.2023.170024.

References

[1] Y.M. Kim, S.K. Kim, Y.J. Lim, N.J. Kim, Effect of microstructure on the yield ratio and low temperature toughness of linepipe steels, ISIJ Int. 42 (2002) 1571–1577, https://doi.org/10.2355/isijinternational.42.1571
[2] X. Li, Y. Liu, K. Gan, J. Dong, C. Liu, Acquiring a low yield ratio well synchronized with enhanced strength of HSLA pipeline steels through adjusting multiple-phase microstructures, Mater. Sci. Eng. A 785 (2020) 139350, , https://doi.org/10.1016/j.msea.2020.139350
[3] B.B. He, M. Wang, L. Liu, M.X. Huang, High-strength medium Mn quenching and partitioning steel with low yield ratio, Mater. Sci. Technol. 35 (2019) 2109–2114, https://doi.org/10.1080/02670836.2019.1566046
[4] Y. Liu, L. Xu, C. Qiu, Development of an additively manufactured metastable beta titanium alloy with a fully equiaxed grain structure and ultrahigh yield strength, Addit. Manuf. 60 (2022) 103208, , https://doi.org/10.1016/j.addma.2022.103208
[5] G. Deng, X. Zhao, L. Su, P. Wei, L. Zhang, L. Zhan, Y. Chong, H. Zhu, N. Tsuji, Effect of high pressure torsion process on the microhardness, microstructure and tribological property of Ti6Al4V alloy, J. Mater. Sci. Technol. 94 (2021) 183–195, https://doi.org/10.1016/j.jmst.2021.03.044
[6] Y. Chong, G. Deng, A. Shibata, N. Tsuji, Microstructure evolution and phase transformation of Ti-1.0 wt%Fe alloy with an equiaxed α + β initial microstructure during high-pressure torsion and subsequent annealing, Adv. Eng. Mater. 21 (2019), https://doi.org/10.1002/adem.201900607
[7] G. Deng, T. Bhattacharjee, Y. Chong, R. Zheng, Y. Bai, A. Shibata, N. Tsuji, Characterization of microstructure and mechanical property of pure titanium with different Fe addition processed by severe plastic deformation and subsequent annealing, IOP Conf. Ser. Mater. Sci. Eng. 194 (2017), https://doi.org/10.1088/1757-899X/194/1/012020
[8] G. Deng, Y. Chong, L. Su, L. Zhan, P. Wei, X. Zhao, L. Zhang, Y. Tian, H. Zhu, N. Tsuji, Mechanisms of remarkable wear reduction and evolutions of subsurface microstructure and nano-mechanical properties during dry sliding of nano-grained Ti6Al4V alloy: a comparative study, Tribol. Int. 169 (2022) 107464, , https://doi.org/10.1016/j.triboint.2022.107464
[9] G. Deng, T. Bhattacharjee, Y. Chong, R. Zheng, Y. Bai, A. Shibata, N. Tsuji, Influence of Fe addition in CP titanium on phase transformation, microstructure and mechanical properties during high pressure torsion, J. Alloy. Compd. 822 (2020) 153604, , https://doi.org/10.1016/J.JALLCOM.2019.153604
[10] Y. Chong, R. Zheng, G. Deng, A. Shibata, N. Tsuji, Investigation on the microstructure and mechanical properties of Ti-1.0Fe alloy with equiaxed α + β microstructures, Metall. Mater. Trans. A. 51 (2020) 2851–2862, https://doi.org/10.1007/s11661-020-05760-x
[11] J. Vishnu, M. Sankar, H.J. Rack, N. Rao, A.K. Singh, G. Manivasagam, Effect of phase transformations during aging on tensile strength and ductility of metastable beta titanium alloy Ti–35Nb–7Zr–5Ta-0.35O for orthopedic applications, Mater. Sci. Eng. A 779 (2020) 139127, , https://doi.org/10.1016/j.msea.2020.139127
[12] D. Kuroda, M. Niinomi, M. Morinaga, Y. Kato, T. Yashiro, Design and mechanical properties of new β type titanium alloys for implant materials, Mater. Sci. Eng. A 243 (1998) 244–249, https://doi.org/10.1016/s0921-5093(97)00808-3
[13] Y.L. Hao, S.J. Li, S.Y. Sun, C.Y. Zheng, Q.M. Hu, R. Yang, Super-elastic titanium alloy with unstable plastic deformation, Appl. Phys. Lett. 87 (2005) 91906, https://doi.org/10.1063/1.2037192
[14] X.L. Zhao, M. Niinomi, M. Nakai, G. Miyamoto, T. Furuhara, Microstructures and mechanical properties of metastable Ti–30Zr–(Cr, Mo) alloys with changeable Young's modulus for spinal fixation applications, Acta Biomater. 7 (2011) 3230–3236, https://doi.org/10.1016/j.actbio.2011.04.019
[15] J. Gao, Y. Huang, D. Guan, A.J. Knowles, L. Ma, D. Dye, W.M. Rainforth, Deformation mechanisms in a metastable beta titanium twinning induced plasticity alloy with high yield strength and high strain hardening rate, Acta Mater. 152 (2018) 301–314, https://doi.org/10.1016/j.actamat.2018.04.035
[16] J.M. Oh, C.H. Park, J.T. Yeom, J.K. Hong, N. Kang, S.W. Lee, High strength and ductility in low-cost Ti–Al–Fe–Mn alloy exhibiting transformation-induced plasticity, Mater. Sci. Eng. A 772 (2020) 138813, , https://doi.org/10.1016/j.msea.2019.138813
[17] M. Ahmed, D. Wexler, G. Casillas, O.M. Ivasishin, E.V. Pereloma, The influence of β phase stability on deformation mode and compressive mechanical properties of Ti-10V–3Fe-3Al alloy, Acta Mater. 84 (2015) 124–135, https://doi.org/10.1016/j.actamat.2014.10.043
[18] X.L. Zhao, M. Niinomi, M. Nakai, T. Ishimoto, T. Nakano, Development of high Zr-containing Ti-based alloys with low Young's modulus for use in removable implants, Mater. Sci. Eng. C 31 (2011) 1436–1444, https://doi.org/10.1016/j.msec.2011.05.013
[19] X.L. Zhao, L. Li, M. Niinomi, M. Nakai, D.L. Zhang, C. Suryanarayana, Metastable Zr–Nb alloys for spinal fixation rods with tunable Young's modulus and low magnetic resonance susceptibility, Acta Biomater. 62 (2017) 372–384, https://doi.org/10.1016/j.actbio.2017.08.026
[20] R.P. Kolli, W.J. Joost, S. Ankem, Phase stability and stress-induced transformations in beta titanium alloys, JOM 67 (2015) 1273–1280, https://doi.org/10.1007/s11837-015-1411-y
[21] M.H. Cai, C.Y. Lee, Y.K. Lee, Effect of grain size on tensile properties of fine-grained metastable β titanium alloys fabricated by stress-induced martensite and its reverse transformations, Scr. Mater. 66 (2012) 606–609, https://doi.org/10.1016/j.scriptamat.2012.01.015
[22] J.F. Xiao, X.K. Shang, Y. Li, Q.W. Guan, B. He, Grain size-dependent tensile behavior in a metastable beta titanium alloy, Mater. Sci. Technol. (2022) 469–483, https://doi.org/10.1080/02670836.2022.2062637
[23] Z. Liao, B. Luan, X. Zhang, R. Liu, K.L. Murty, Q. Liu, Effect of varying α phase fraction on the mechanical properties and deformation mechanisms in a metastable β-ZrTiAlV alloy, Mater. Sci. Eng. A 772 (2020) 138784, , https://doi.org/10.1016/j.msea.2019.138784
[24] Z. Chen, L. Yang, X. Ma, Q.I. Sun, F. Li, Tensile deformation behavior of a heterogeneous structural dual-phase metastable b titanium alloy, Metall. Mater. Trans. A. 53 (2022) 2754–2767, https://doi.org/10.1007/s11661-022-06705-2
[25] C. Li, X. Wu, J.H. Chen, S. van der Zwaag, Influence of α morphology and volume fraction on the stress-induced martensitic transformation in Ti–10V–2Fe–3Al, Mater. Sci. Eng. A 528 (2011) 5854–5860, https://doi.org/10.1016/j.msea.2011.03.107
[26] C. Li, J. Chen, Y.J. Ren, W. Li, J.J. He, J.H. Chen, Effect of solution heat treatment on the stress-induced martensite transformation in two new titanium alloys, J. Alloy. Compd. 641 (2015) 192–200, https://doi.org/10.1016/j.jallcom.2015.04.070
[27] C. Zhu, X. Zhang, C. Li, C. Liu, K. Zhou, A strengthening strategy for metastable β titanium alloys: Synergy effect of primary α phase and β phase stability, Mater. Sci. Eng. A 852 (2022) 143736, , https://doi.org/10.1016/j.msea.2022.143736
[28] M.C. Zang, H.Z. Niu, H.R. Zhang, H. Tan, D.L. Zhang, Cryogenic tensile properties and deformation behavior of a superhigh strength metastable beta titanium alloy Ti–15Mo–2Al, Mater. Sci. Eng. A 817 (2021) 141344, , https://doi.org/10.1016/J.MSEA.2021.141344
[29] Z. He, N. Jia, H. Wang, H. Yan, Y. Shen, Synergy effect of multi-strengthening mechanisms in FeMnCoCrN HEA at cryogenic temperature, J. Mater. Sci. Technol. 86 (2021) 158–170, https://doi.org/10.1016/j.jmst.2020.12.079
[30] X. Zhao, Y. Wang, H. Xue, N. Jia, Y. Liu, D. Zhang, The effect of strain rate on deformation-induced α′ phase transformation and mechanical properties of a metastable β-type Ti–30Zr–5Mo alloy, J. Alloy. Compd. 894 (2022) 162394, , https://doi.org/10.1016/J.JALLCOM.2021.162394
[31] Z.F. He, N. Jia, H.W. Wang, Y. Liu, D.Y. Li, Y.F. Shen, The effect of strain rate on mechanical properties and microstructure of a metastable FeMnCoCr high entropy alloy, Mater. Sci. Eng. A 776 (2020), https://doi.org/10.1016/j.msea.2020.138982
[32] Z. Liao, B. Luan, X. Zhang, R. Liu, K.L. Murty, Q. Liu, Effect of varying α phase fraction on the mechanical properties and deformation mechanisms in a metastable β-ZrTiAlV alloy, Mater. Sci. Eng. A 772 (2020) 138784, , https://doi.org/10.1016/j.msea.2019.138784
[33] F. Niessen, A.A. Gazder, D.R.G. Mitchell, E.V. Pereloma, In-situ observation of nucleation, growth and interaction of deformation-induced α″ martensite in metastable Ti–10V–2Fe–3Al, Mater. Sci. Eng. A 802 (2020) 140237, , https://doi.org/10.1016/j.msea.2020.140237
[34] E. Kobayashi, M. Ando, Y. Tsutsumi, H. Doi, T. Yoneyama, M. Kobayashi, T. Hanawa, Inhibition effect of zirconium coating on calcium phosphate precipitation of titanium to avoid assimilation with bone, Mater. Trans. 48 (2007) 301–306, https://doi.org/10.2320/matertrans.48.301
[35] X. Sun, D. Liu, M. Chen, W. Zhou, N. Nomura, T. Hanawa, Influence of annealing treatment on the microstructure, mechanical performance and magnetic susceptibility of low magnetic Zr–1Mo parts manufactured via laser additive manufacturing, Mater. Sci. Eng. A 804 (2021) 140740, , https://doi.org/10.1016/j.msea.2021.140740
[36] R. Xue, D. Wang, Y. Tian, J. Wang, L. Liu, L. Zhang, Zr-xNb-4Sn alloys with low Young's modulus and magnetic susceptibility for biomedical implants, Prog. Nat. Sci. Mater. Int. 31 (2021) 772–778, https://doi.org/10.1016/j.pnsc.2021.09.008
[37] Z.W. Zhu, C.Y. Xiong, J. Wang, R.G. Li, Y. Ren, Y.D. Wang, Y. Li, In situ synchrotron X-ray diffraction investigations of the physical mechanism of ultra-low strain

hardening in Ti–30Zr–10Nb alloy, Acta Mater. 154 (2018) 45–55, https://doi.org/10.1016/j.actamat.2018.05.034
[38] X.L. Zhao, M. Niinomi, M. Nakai, Relationship between various deformation-induced products and mechanical properties in metastable Ti–30Zr–Mo alloys for biomedical applications, J. Mech. Behav. Biomed. Mater. 4 (2011) 2009–2016, https://doi.org/10.1016/j.jmbbm.2011.06.020
[39] A. Maghsoudlou, A. Zarei-Hanzaki, H.R. Abedi, A. Barabi, F. Pilehva, D. Dietrich, T. Lampke, The room temperature tensile deformation behavior of thermo-mechanically processed β-metastable Ti–Nb–Ta–Zr bio-alloy: the role of deformation-induced martensite, Mater. Sci. Eng. A 738 (2018) 15–23, https://doi.org/10.1016/j.msea.2018.09.038
[40] X. Ma, Z. Chen, L. Xiao, W. Lu, S. Luo, Y. Mi, Compressive deformation of a metastable β titanium alloy undergoing a stress-induced martensitic transformation: the role of β grain size, Mater. Sci. Eng. A 794 (2020) 139919, , https://doi.org/10.1016/j.msea.2020.139919
[41] F. Brunke, C. Siemers, J. Rösler, Second-generation titanium alloys Ti–15Mo and Ti–13Nb–13Zr: a comparison of the mechanical properties for implant applications, MATEC Web Conf. 321 (2020) 05006, https://doi.org/10.1051/matecconf/202032105006
[42] J. Wang, Y. Zhao, W. Zhou, Q. Zhao, S. Huang, W. Zeng, In-situ investigation on tensile deformation and fracture behaviors of a new metastable β titanium alloy, Mater. Sci. Eng. A 799 (2021) 140187, , https://doi.org/10.1016/j.msea.2020.140187
[43] H. Lu, P. Ji, B. Li, W. Ma, B. Chen, X. Zhang, X. Zhang, M. Ma, R. Liu, Mechanical properties and deformation mechanism of a novel metastable β-type Ti–4V–2Mo–2Fe alloy, Mater. Sci. Eng. A 848 (2022) 143376, , https://doi.org/10.1016/j.msea.2022.143376
[44] Y.M. Wang, E. Ma, Strain hardening, strain rate sensitivity, and ductility of nanostructured metals, Mater. Sci. Eng. A 375–377 (2004) 46–52, https://doi.org/10.1016/j.msea.2003.10.214
[45] X. Zhao, S. Li, M. Zhang, Y. Liu, T.B. Sercombe, S. Wang, Y. Hao, R. Yang, L.E. Murr, Comparison of the microstructures and mechanical properties of Ti–6Al–4V fabricated by selective laser melting and electron beam melting, Mater. Des. 95 (2016) 21–31, https://doi.org/10.1016/j.matdes.2015.12.135
[46] S.C. Wang, M. Aindow, M.J. Starink, Effect of self-accommodation on α / α boundary boundary populations in pure titanium, Acta Mater. 51 (51) (2003) 2485–2503, https://doi.org/10.1016/S1359-6454(03)00035-1
[47] L. Chai, B. Chen, Z. Zhou, K.L. Murty, Y. Ma, W. Huang, A special twin relationship or a common Burgers misorientation between α plates after β quenching in Zr alloy, Mater. Charact. 104 (2015) 61–65, https://doi.org/10.1016/j.matchar.2015.04.008
[48] S. Zhang, Q. Wang, G. Li, Y. Liu, D. Li, Correlation between heat-treatment windows and mechanical properties of high-temperature titanium alloys Ti-60, Acta Metall. Sin. 38 (2002) 70–73.
[49] F. Sun, J. Li, H. Kou, B. Tang, H. Chang, J. Cai, L. Zhou, α phase solution kinetics and solution microstructure characteristics of Ti60 titanium alloy, Chin. J. Nonferr. Met. 20 (2010) s437–s440.
[50] Y. Chong, G. Deng, S. Gao, J. Yi, A. Shibata, N. Tsuji, Yielding nature and Hall-Petch relationships in Ti-6Al-4V alloy with fully equiaxed and bimodal microstructures, Scr. Mater. 172 (2019) 77–82, https://doi.org/10.1016/j.scriptamat.2019.07.015
[51] X. Wu, B. Zhang, Y. Zhang, H. Niu, D. Zhang, Manipulating the strength and tensile ductility of a PM near α titanium alloy by adjusting the morphologies and volume fractions of α and β_t domains, Mater. Sci. Eng. A 859 (2022) 144184, , https://doi.org/10.1016/j.msea.2022.144184
[52] J. Umeda, T. Tanaka, T. Teramae, S. Kariya, J. Fujita, H. Nishikawa, Y. Shibutani, J. Shen, K. Kondoh, Microstructures analysis and quantitative strengthening evaluation of powder metallurgy Ti–Fe binary extruded alloys with (α+β)-dual-phase, Mater. Sci. Eng. A 803 (2021) 140708, , https://doi.org/10.1016/j.msea.2020.140708
[53] E. Cerri, E. Ghio, G. Bolelli, Effect of surface roughness and industrial heat treatments on the microstructure and mechanical properties of Ti6Al4V alloy manufactured by laser powder bed fusion in different built orientations, Mater. Sci. Eng. A 851 (2022) 143635, , https://doi.org/10.1016/j.msea.2022.143635
[54] D.R.N. Correa, P.A.B. Kuroda, M.L. Lourenço, C.J.C. Fernandes, M.A.R. Buzalaf, W.F. Zambuzzi, C.R. Grandini, Development of Ti–15Zr–Mo alloys for applying as implantable biomedical devices, J. Alloy. Compd. 749 (2018) 163–171, https://doi.org/10.1016/j.jallcom.2018.03.308
[55] P. Akira, B. Kuroda, M. Afonso, R. Buzalaf, C. Roberto, Effect of molybdenum on structure, microstructure and mechanical properties of biomedical Ti–20Zr–Mo alloys, Mater. Sci. Eng. C 67 (2016) 511–515, https://doi.org/10.1016/j.msec.2016.05.053
[56] J. Lu, Y. Zhao, P. Ge, H. Niu, Microstructure and beta grain growth behavior of Ti –Mo alloys solution treated, Mater. Charact. 84 (2013) 105–111, https://doi.org/10.1016/j.matchar.2013.07.014
[57] R. Suyalatu, Y. Kondo, H. Tsutsumi, N. Doi, T. Nomura, Hanawa, Effects of phase constitution on magnetic susceptibility and mechanical properties of Zr-rich Zr–Mo alloys, Acta Biomater. 7 (2011) 4259–4266, https://doi.org/10.1016/j.actbio.2011.07.005
[58] P. Tsipouridis, L. Koll, C. Krempaszky, E. Werner, On the strength of grain and phase boundaries in ferritic-martensitic dual-phase steels, Int. J. Mater. Res. 102 (2011) 674–686, https://doi.org/10.3139/146.110519
[59] Y. Fu, W. Xiao, J. Wang, L. Ren, X. Zhao, C. Ma, A novel strategy for developing α + β dual-phase titanium alloys with low Young's modulus and high yield strength, J. Mater. Sci. Technol. 76 (2021) 122–128, https://doi.org/10.1016/J.JMST.2020.11.018
[60] S.W. Lee, J.M. Oh, C.H. Park, J.K. Hong, J.T. Yeom, Deformation mechanism of metastable titanium alloy showing stress-induced α′-martensitic transformation, J. Alloy. Compd. 782 (2019) 427–432, https://doi.org/10.1016/j.jallcom.2018.12.160